Evidence of solar wind irradiation on mineral grains embedded in matrix of the Northwest Africa 801 CR chondrite

Sohei Wada [a, *], Ken-ichi Bajo [a], Tomoya Obase [a,b], Hisayoshi Yurimoto [a]

[a] *Department of Natural History Sciences, Hokkaido University, Sapporo, Hokkaido 060-0810, Japan*

[b] *Department of Earth and Planetary Sciences, Institute of Science Tokyo, Meguro, Tokyo, 152-8551, Japan*

* Corresponding author: Sohei Wada

Tel: +81-11-706-9174

E-mail: sohei@ep.sci.hokudai.ac.jp

Keywords: Solar wind; Helium; Carbonaceous chondrites; Isotope imaging

ABSTRACT

Solar wind (SW) is preserved in meteorites as abundant solar noble gases. We performed *in situ* ^{4}He isotope imaging of mineral grains in the CR2 chondrite matrix of Northwest Africa 801 (NWA 801) using time-of-flight secondary neutral mass spectrometry with strong-field post-ionization. $^{4}He^{+}$ signals were detected along the surfaces of individual grains of Fe-Ni metal, ferrihydrite, olivine, pyroxene, and troilite. The high ^{4}He concentrations along the surfaces indicate implantation of SW into the mineral grains. We determined the SW-^{4}He fluence of eight mineral grains from the line profiles across the grain boundaries. SW-^{4}He fluence ranged from 2.7×10^{16} to 58×10^{16} atoms cm^{-2}. These fluences were then used to calculate the SW irradiation durations. Assuming irradiation occurred at 4 astronomical units, the durations ranged from 3.8 to 82 kyr. These durations correspond to the residence time of individual mineral grains on the surface of the parent body. The variation in residence time for the mineral grains suggests variable durations for local mixing and burial processes on the parent body. The SW exposure ages provide insights into the gardening rate driven by small-scale impact mixing processes on the parent body.

1. INTRODUCTION

Evidence for solar wind (SW) implantation was first observed in the Khor Temiki aubrite meteorite (Eberhardt et al., 1965), classified as a gas-rich meteorite. Analysis of this meteorite revealed a negative correlation between noble gas concentrations and grain sizes for minerals in the matrix. Noble gas concentrations in different grain-size fractions of the aubrite were proportional to the surface-to-volume ratio, except for cosmogenic ^{3}He and ^{21}Ne. Similar correlations were observed in lunar samples (e.g., Hintenberger et al., 1970, 1971), suggesting that individual grains are enriched with SW noble gases on their surfaces.

Another approach to confirming SW implantation in grain surfaces is closed system step etching (CSSE) gas extraction, which employs acid leaching to extract noble gases from the surface layers of minerals. CSSE-based noble gas analysis of gas-rich chondrites has shown that He- and Ne-rich components were released in the early etching steps, indicating their presence in the surface layers (Becker et al., 1998; Wieler et al., 2000; Riebe et al., 2017), and similar isotopic compositions to SW for He and Ne (Geiss et al., 1972; Heber et al., 2009). The ^{4}He/^{36}Ar and ^{20}Ne/^{36}Ar ratios in most gas-rich meteorites are lower than the SW ratios, indicating escape of He and Ne from the meteorites after SW implantation (Wieler et al., 1989; Lipschutz et al., 1993). On the other hand, the ^{4}He/^{36}Ar and ^{20}Ne/^{36}Ar ratios of Fe-Ni metal in the gas-rich chondrites are nearly identical to the SW ratios, indicating that SW-He and -Ne in Fe-Ni metal are particularly retentive than those in silicates (Murer et al., 1997). These CSSE

52 results provide evidence that SW noble gases are trapped in the near-surface layers of minerals
53 via ion implantation.
54 *In situ* analysis can clarify the location and concentration of SW noble gases, and
55 their distribution can be compared with petrographic observations. The conventional in situ
56 noble gas analysis approach with laser ablation has achieved sub-millimeter-scale analysis of
57 SW noble gases in meteorites. Nakamura et al. (1999) showed that SW noble gases are enriched
58 in the clastic matrix but not in the pristine matrix of CM chondrites. *In situ* analysis with
59 secondary neutral mass spectrometry (SNMS) achieved micrometer-scale ^{4}He analysis in solid
60 materials (Bajo et al., 2015, 2016). Through laser ionization mass nanoscope (LIMAS) analysis,
61 Bajo et al. (2024) showed that SW-^{4}He was highly heterogeneously distributed grain by grain
62 in the clastic matrix of a gas-rich meteorite, Northwest Africa 801 (NWA 801) CR2 chondrite.
63 However, *in situ* analyses have not yet demonstrated that the SW-implanted ^{4}He resides at the
64 very grain surface. NWA 801 contains a large amount of SW noble gases, about one order of
65 magnitude higher than in other solar-gas-rich CR chondrites (Bischoff et al., 1993; Scherer and
66 Schultz, 2000; Obase et al. 2021). Bajo et al. (2024) showed high ^{4}He concentration spots in
67 the polished section of NWA 801. Nakashima et al. (2009) mentioned that NWA 852, the paired
68 meteorite of NWA 801, was exposed to galactic cosmic rays on the parent body for several tens
69 of million years. The previous studies suggest that NWA 801 preserves the regolith
70 environments of the CR chondrite parent body.

In this study, we conducted *in situ* analysis of the ^{4}He isotope distribution using LIMAS in individual mineral grains embedded in the NWA 801 section at a sub-micrometer spatial resolution, revealing the distribution of SW-^{4}He on the surface region of individual mineral grains. Furthermore, the SW irradiation duration for each mineral and the implications for the history of regolith formation on the parent body are discussed.

2. MATERIALS AND METHODS

2.1. Sample preparation and electron microscopy

A polished section of the NWA 801 meteorite was used in this study. A chip of the chondrite, embedded in an epoxy resin disk, was polished using an automatic polishing machine (MA-200e, Musashino Denshi) at Hokkaido University. The polished section was then cut into a 5 × 7 × 1 mm³ cuboid using a low-speed diamond saw (IsoMet Low Speed, Buehler) for placement in a sample holder. To minimize degassing, the cut specimen was immersed in acetone for 1 day to remove the epoxy resin. Finally, the specimen surface was coated with an approximately 10 nm thick gold film via vacuum deposition.

Backscattered electron (BSE) images of the sample were obtained using a field emission scanning electron microscope (FE-SEM; JSM-7000F, JEOL) at Hokkaido University to characterize the petrography prior to isotope-imaging analysis. Quantitative elemental analysis and X-ray elemental mapping were performed using an energy-dispersive X-ray

spectrometer (EDS; X-Max 150, Oxford) attached to the FE-SEM. A 15 keV electron beam probe was used with a current of 4 nA.

2.2. Helium isotope analysis

He isotope analysis was conducted using an SNMS (LIMAS, JEOL) at Hokkaido University (Bajo et al., 2024). In this study, we used a finer primary $^{69}Ga^{+}$ beam of 1 nA than that of Bajo et al. (2024) of 40 nA to achieve *in situ* analysis with a sub-micrometer spatial resolution. The primary ion beam with an energy of 30 keV was pulsed in 200 ns and focused onto the sample surface. The sample surface was inclined at 55° to the primary beam, resulting in a vertical beam diameter 1.7 times larger than the horizontal diameter.

Sputtered neutrals were photoionized under strong-field ionization conditions using a focused femtosecond laser (~5.5 mJ, Astrella, Coherent) installed in LIMAS and operating at a 1 kHz repetition rate. The laser was focused at a 30 μm diameter spot approximately ~50 μm above the sample surface. Ions with m/z 4 ($^{4}He^{+}$), 12 ($^{24}Mg^{2+}$), 16 ($^{32}S^{2+}$), 18.6 ($^{56}Fe^{3+}$), and 28 ($^{56}Fe^{2+}$, $^{28}Si^{+}$) were measured using a multi-turn time-of-flight (TOF) mass spectrometer, "MULTUM II" (Okumura et al., 2004; Tonotani et al., 2016), with an acceleration voltage of −5 kV. The ion-injection system parameters for MULTUM II were optimized for high ion-transmission efficiency based on the study by Tonotani et al. (2016). The flight time was adjusted to achieve a mass resolving power of ~20,000 (calculated using $T/2\Delta T$) for m/z 4. Interference ions, such as $^{12}C^{3+}$ and $^{16}O^{4+}$ for $^{4}He^{+}$, were removed using ion

gates in the MULTUM II ion trajectory. A typical TOF mass spectrum from the sample is shown in Fig. 1. To obtain a 2D isotope image, the primary beam was scanned horizontally and vertically at 100 nm intervals. Each point in the image represents a pixel, and 600–6000 TOF mass spectra were collected for each pixel. The analytical conditions for the isotope-imaging analysis are summarized in Table 1.

The background signal of ^{4}He (hereafter referred to as blank ^{4}He) originates from residual ^{4}He gas above the sample surface. This was measured without the primary beam pulse after each isotope-imaging run. The (1–2) × 10^{6} TOF spectra were collected to determine the blank ^{4}He intensity, which varied with analytical conditions, ranging from 1 × 10^{-4} to 1 × 10^{-5} ion counts per mass spectrum scan (cpms). The background signals of ^{56}Fe, ^{24}Mg, and ^{32}S are negligible compared to their signals from the sample.

2.3. Spatial resolution of isotope-imaging analysis

The spatial resolution for individual ion images was determined using line scan profiles of $^{56}Fe^{2+}$ and $^{24}Mg^{2+}$ (Figs. S1–S6) and $^{4}He^{+}$ (Figs. 3–8) across the interface between individual mineral grain and fine-grained groundmass, defined by the 16–84% criterion (Nagata et al., 2019). This is equivalent to the ±1σ criterion for a Gaussian beam. The spatial resolutions for the individual analyses are listed in Table 2. Because the spatial resolutions calculated from the $^{56}Fe^{2+}$ and $^{24}Mg^{2+}$ profiles are broadened by the interface–surface angle, and the ^{4}He layer is narrower than 100 nm (see Section 4.2), the spatial resolution of the image

128 in this study is defined as the width of the ^{4}He layer. The resolutions varied with individual
129 images: 100 nm for Areas 1, 2 and 3, 150 nm for Area 6 and 240 nm for Areas 4 and 5.

130 **2.4. Quantification of ^{4}He concentration**

131 To determine the ^{4}He concentration in the sample, a ^{4}He-implanted Fe-Ni alloy
132 ($Fe_{0.55}Ni_{0.45}$) plate was prepared as a standard, with an implantation dose of 3×10^{15} atoms
133 cm^{-2} at an energy of 20 keV. The ^{4}He-implanted Fe-Ni standard was analyzed using LIMAS
134 with a 30 keV and 32 nA $^{69}Ga^{+}$ primary ion beam, delivered in 400 ns pulses. A 30 × 30 pixel
135 area (12 × 20 μm^2) was scanned, and 100 TOF mass spectra were collected per pixel. Depth
136 profiles of $^{4}He^{+}$, $^{56}Fe^{2+}$, and $^{58}Ni^{2+}$ were obtained from the central 5 × 5 pixels to minimize
137 crater edge effects. Other measurement conditions were identical to those used for sample
138 analysis. Following depth profiling, the crater depth was measured using a confocal laser
139 microscope (VK-X200, Keyence).

140 Since the ion intensity is proportional to the primary beam current, we calculate
141 the ^{4}He concentration using the ratio of the primary beam currents between the isotope imaging
142 and the Fe-Ni standard measurement to correct for the ^{4}He concentration calculations in the
143 sample. Because photoionization by a focused fs laser is less sensitive to matrix effects caused
144 by differences in ionization efficiency depending on the sample material, the ^{4}He concentration
145 was calculated using the following equation, adapted from Bajo et al. (2024):

146 $$[\,^{4}\mathrm{He}] = \left(\,^{4}\mathrm{He}^{+}\right)_{meas} / I_{p1} \times SF^{\mathrm{He}} \quad (1)$$

where [^{4}He], $^4He^+_{meas}$, I_{p1}, and SF^{He} denote the ^{4}He concentration in the measuring volume of a single pixel (atoms cm^{-3}), measured ^{4}He intensities (cpms), primary beam currents for sample, and sensitivity factor for ^{4}He (atoms cm^{-3} cpms^{-1}), respectively. The SF^{He} is derived from the standard analysis as follows:

$$SF^{He} = \frac{\phi \times n}{\sum_{k=1}^{n}\left(\left(\,^4He^+\right)_{meas} - \left(\,^4He^+\right)_{bg}\right)_k / I_{p2} \times d} \quad (2)$$

where Φ, k, and I_{p2}, d denote the ^{4}He fluence (atoms cm^{-2}) for the standard, number of measurement layer (from 1 to n), primary beam currents for standard, and sputtered crater depth (cm), respectively. Additionally, $(^4He^+)_{bg}$ denotes the blank ^{4}He.

3. RESULTS

3.1. Petrography of measurement areas

NWA 801 is classified as a CR2 chondrite (Connolly et al., 2007) and is highly enriched in SW noble gases (Obase et al., 2021). BSE and X-ray elemental images of the polished section of NWA 801 are shown in Fig. 2. SEM analysis reveals that the NWA 801 section contains millimeter-sized chondrules and their fragments embedded in matrix. Pervasive rust veins, primarily composed of ferrihydrite, which are typical terrestrial weathering products, are evident throughout the sample. The matrix contains mineral grains of Fe-Ni metal, ferrihydrite, olivine, pyroxene, and troilite, ranging from approximately 1 to 50 μm. These mineral grains are surrounded by a fine-grained groundmass typically less than 0.1

μm in size (Fig. 2c). Fe-Ni metal and troilite also occur within chondrule interiors and rims. Some Fe-Ni metal grains have been partially or completely replaced by ferrihydrite. In this study, we examined the mineral grains and the surrounding fine-grained groundmass in Areas 1–6, as shown in Fig. 2a.

3.2. ^{4}He distribution of mineral grains

Enlarged BSE and $^{4}He^{+}$ images of Areas 1–6 are shown in Figs. 3–8. The ion images reveal that the mineral grains (<50 μm in size) of Fe-Ni metal (Figs. 3–5), ferrihydrite (Figs. 4–7), olivine (Figs. 3, 6, and 8), pyroxene (Figs. 3, 6, and 7), and troilite (Fig. 3–8) are enriched in ^{4}He along part of their grain-surface contours. These mineral grains are embedded in a fine-grained groundmass. Line scans of $^{56}Fe^{2+}$ and $^{24}Mg^{2+}$ across a few selected grain boundaries illustrate the relationships between the boundaries and ^{4}He-concentrated regions. These line scans were obtained from a location with a high $^{4}He^{+}$ intensity to determine the largest fluence of SW irradiation of the grain.

Fe-Ni metal

Three Fe-Ni metal grains can be observed (Figs. 3–5) in Areas 1–3 (Fig. 2). In Area 1, the Fe-Ni metal grain is approximately 20 × 20 μm^2 (Fig. 3a). $^{4}He^{+}$ signals were detected along the grain edge, except for the lower right edge (Fig. 3b). Intensity changes in the line profiles for $^{56}Fe^{2+}$ and $^{24}Mg^{2+}$ delineate the grain boundary (Fig. 3c). Similar profile changes are observed for the other Fe-Ni metal grains (Figs. 4c, 4d, and 5c). The $^{4}He^{+}$ signal

appears as a peak at the metal–groundmass interface with a width of 100 nm, defined as the full width at $e^{-\frac{1}{2}}$ height of the $^4He^+$ peak maximum, equivalent to ±1σ for a Gaussian distribution. The peak ^4He concentration is 6.4×10^{21} atoms cm^{-3} (Fig. 3c), and the $^4He^+$ signals are below the detection limit in the metal's interior and the surrounding groundmass.

In Area 2, the Fe-Ni metal grain is approximately 5 × 7 μm^2 (Fig. 4a). $^4He^+$ signals are detected along the grain edge, except for the center-left edge (Fig. 4b). The $^4He^+$ profile exhibits a single peak with a 100 nm width (±1σ) at the narrow distribution of the metal–groundmass interface. The peak ^4He concentration is 3.1×10^{21} atoms cm^{-3} (Fig. 4c), and the $^4He^+$ signals are below the detection limit in the metal's interior and the surrounding groundmass. The $^4He^+$ peak width in Line C–D (Fig. 4d) is wider than that in Line A–B (Fig. 4c), and a ^4He peak is observed within the Fe-Ni metal. This wider $^4He^+$ distribution in Line C–D is attributed to the diagonal polishing of the grain edge.

In Area 3, the Fe-Ni metal grain is approximately 20 × 30 μm^2 (Fig. 5a). $^4He^+$ signals can be partially observed along the grain edge (Fig. 5b), whereas other areas are below the detection limit. The $^4He^+$ profile exhibits a single 100 nm wide peak (±1σ). The peak ^4He concentration is 2.2×10^{21} atoms cm^{-3} (Fig. 5c).

Ferrihydrite

Two ^4He-rich ferrihydrite grains can be observed (Figs. 6 and 7) in Areas 4 and 5 (Fig. 2). In Area 4, the grain is approximately 10 × 15 μm^2 (Fig. 6a), and $^4He^+$ signals were

detected along its edge (Fig. 6b). Line profiles of $^{4}He^{+}$, $^{56}Fe^{2+}$, and $^{24}Mg^{2+}$ across the grain boundary exhibit significant intensity changes at the boundary (Fig. 6c). The $^{4}He^{+}$ profile shows a single 250 nm wide peak (±1σ), and the peak ^{4}He concentration is 17.0×10^{21} atoms cm^{-3} (Fig. 6c). The $^{4}He^{+}$ signals are below the detection limit in the ferrihydrite's interior, whereas weak ^{4}He intensities are detectable in the groundmass, with small ^{4}He-enriched spots (Fig. 6b).

In Area 5, the ferrihydrite grain is approximately 7×8 μm^2 (Fig. 7a), and $^{4}He^{+}$ signals are detected along its edge (Fig. 7b). Line profiles of $^{56}Fe^{2+}$ and $^{24}Mg^{2+}$ (Fig. 7c) show similar changes at the grain boundary as those observed in the ferrihydrite grain in Area 4. The $^{4}He^{+}$ profile shows a single 240 nm wide peak (±1σ), and the peak ^{4}He concentration is 0.6×10^{21} atoms cm^{-3} (Fig. 7g). The $^{4}He^{+}$ signals in the ferrihydrite's interior are below the detection limit.

Although ferrihydrite grains were also present in Areas 2 and 3, detectable $^{4}He^{+}$ were not observed at the grain boundaries or within the grains (Figs. 4 and 5).

Olivine and pyroxene

^{4}He-rich olivine and pyroxene grains were observed in the $^{4}He^{+}$ images of Areas 4 and 5, as shown in Figs. 6 and 7, respectively. In Area 4, the olivine grain is approximately 3 $\times$ 2 μm^2 (Fig. 6a), and $^{4}He^{+}$ signals are detected along its edge (Fig. 6b). The line profiles show a ^{4}He peak at the grain boundary (Fig. 6d) with a width of 230 nm (±1σ) and a peak

concentration of 0.9×10^{21} atoms cm^{-3} (Fig. 6d). The $^4He^+$ signals in the olivine's interior were below the detection limit, whereas the pyroxene grains in this area exhibited no detectable $^4He^+$ signals.

In Area 5, the pyroxene grain is approximately 2×1 μm^2 (Fig. 7a), and ^4He is observed along its edge (Fig. 7b). The $^4He^+$ peak in the line profile appears at the grain boundary with a width of 240 nm ($\pm 1\sigma$) (Fig. 7c) and a peak concentration of 0.7×10^{21} atoms cm^{-3} (Fig. 7h). The $^4He^+$ signals in the pyroxene's interior were below the detection limit and no ^4He was detected within other pyroxene grains in Area 5.

Troilite

Four ^4He-rich troilite grains were observed in the $^4He^+$ images of Areas 2, 4, 5, and 6, as shown in Figs. 4, 6, 7, and 8. The largest troilite grain of approximately 5×5 μm^2 (Fig. 8a) was observed in Area 6, and $^4He^+$ signals were detected along its edge, except for the upper and left edges (Fig. 8b). Line scans of $^4He^+$, $^{56}Fe^{2+}$, and $^{24}Mg^{2+}$ across the grain boundary were conducted to analyze the ^4He-concentrated region. As shown in Fig. 8c, a $^4He^+$ peak appears at the grain boundary with a width of 150 nm ($\pm 1\sigma$) and concentration of 2.5×10^{21} atoms cm^{-3} (Fig. 8c). However, ^4He is not detected within the grain or the surrounding fine-grained groundmass. The ^4He concentrations of the troilite grains in Areas 2, 4, and 5 are 2.9×10^{21}, 10.9×10^{21}, and 2.7×10^{21} atoms cm^{-3}, respectively. These grains are attached to ferrihydrite grains. Because the sizes of these grains were smaller than the spatial resolution of

the analysis, the spatial distributions of ^{4}He within them could not be determined.

Fine-grained groundmass

All areas imaged in this study contained a fine-grained groundmass surrounding the mineral grains. In Areas 4 and 5, $^4He^+$ signals were detected from the groundmass (Figs. 6 and 7), with a typical concentration of approximately 0.6×10^{21} atoms cm^{-3}. ^{4}He-rich spots with concentrations of $1.8–8.4 \times 10^{21}$ atoms cm^{-3} were also observed, often corresponding to S and Fe enrichments (Figs. 6 and 7), suggesting that they represent fine-grained iron sulfides. The areas with $\sim 0.6 \times 10^{21}$ atoms cm^{-3} (blue areas in Fig. 6b, 6f, and 7b) appeared to be composed mainly of fine-grained silicates, having a concentration is similar to the peak concentrations of the olivine and pyroxene grains (Figs. 6d and 7h). By contrast, $^4He^+$ signals were not detected from the groundmass in Areas 1–3 and 6 (Figs. 3–5, 8). Therefore, we conclude that ^{4}He content varies significantly within the groundmass.

4. DISCUSSION

4.1. Evidence of SW implantation

The line profiles of the mineral grains showed that the $^4He^+$ signals characteristically originated from the grain boundaries (Figs. 3–8). These distributions suggest that the ^{4}He is trapped either in the crystal edges or in the fine-grained groundmass attached to the crystals. In the former case, the trapped ^{4}He would be located at shallower depths than the

spatial resolution of the image (~100 nm) from the crystal surface. Otherwise, the fine-grained groundmass, smaller than 100 nm, would contain ^{4}He.

The $^4He^+$ signals on the diagonally polished edge of the Fe-Ni metal grain demonstrated that the peak position is within the metal (Fig. 4d), providing evidence that ^{4}He is trapped within the metal itself. We first observe abundant ^{4}He at the grain surface due to the SW implantation into the grain of the meteorite. The ^{4}He images shown in Figs. 6 and 7 also validate that the ^{4}He peaks are within the minerals rather than the groundmass. By contrast, no observations showed groundmass containing ^{4}He concentrations comparable to the ^{4}He peaks at the grain boundaries. The ^{4}He concentration in the groundmass was one to two orders of magnitude lower than that in the ^{4}He peaks at the grain boundaries. Therefore, it is plausible that ^{4}He is trapped at shallow depths from the surfaces of the mineral grains. The spatial resolution of the isotope images is not sufficient to observe the shallow SW implantation depth of approximately 20–40 nm from the surface of the minerals, which is expected by the TRIM (the Transport of Ions in Matter) code (Ziegler et al., 2012).

The ^{4}He-enriched layer beneath the grain surface, less than 100 nm thick, can be produced through ion implantation with kinetic energies of ~keV/nucleon (Futagami et al., 1990; Kuhlman et al., 2015; Wiens et al., 2004; Grimberg et al., 2008; Bajo et al. 2015). In interplanetary space, such low-energy ions are delivered by the SW. The ^{4}He enrichment observed within 100 nm for the Fe-Ni metal grains (Fig. 3c) is consistent with the typical SW

range of 20–40 nm from the surface. Therefore, we conclude that the ^{4}He line profiles in Figs. 3–8 provide direct evidence of SW implantation into the mineral grains. These grains were exposed to SW on the surface of the parent body and mechanically mixed with other meteorite precursor materials (Hashiguchi et al., 2013) to form the current structure of NWA 801 by subsequent compaction in the parent body (Charles et al., 2018).

Additionally, abundant SW-^{4}He was observed at the edges of the ferrihydrite grains (Figs. 6 and 7). Ferrihydrite is a typical terrestrial weathering product (Noguchi, 1994), and trapped light noble gases are considered to be released during terrestrial weathering (Scherer et al., 1994; Stelzner et al., 1999; Bland et al., 2006). The presence of SW-^{4}He in ferrihydrite suggests that the implanted ^{4}He remained in the ferrihydrite even though the original phase, likely metal, weathered to ferrihydrite on Earth. Another interpretation is that the ferrihydrite formed during aqueous alteration on the parent body, similar to that suggested for CI chondrites by Tomeoka and Buseck (1988). In this scenario, the altered ferrihydrite grains were exposed to SW on the parent body after formation. The results of this study do not allow us to determine which process is more plausible for the formation of ferrihydrite grains. However, in either case, the ^{4}He distributions in the ferrihydrite grains were produced by SW irradiation.

Bajo et al. (2024) using micrometer ^{4}He analysis firstly showed that ^{4}He is highly concentrated and sparsely scattered in the matrix in a gas-rich meteorite. This study advanced

299 their findings through sub-micrometer ^{4}He analysis and is the first to identify the ^{4}He
300 concentrated on the surfaces of individual mineral grains. Thus, it provides direct evidence for
301 SW implantation into the constituent minerals of the meteorite. Furthermore, the observed
302 heterogeneity of SW-^{4}He implantation may be related to the regolith formation dynamics on
303 the parent body.

304 **4.2. SW-^{4}He fluence in mineral grains**

305 Because the ^{4}He was implanted by SW irradiation (with a typical energy of ~1
306 keV/nucleon), the actual peak width should be several tens of nanometers. The observed line
307 profiles (Figs. 3–8) were likely broader than the true profiles and exhibited lower peak
308 concentrations because of the ~100 nm spatial resolution of the images. However, the integral
309 of the ^{4}He concentrations in each line profile represents the total amount of ^{4}He in the sputtered
310 volume. Therefore, the SW-^{4}He fluence, Φ_{sample}, can be calculated from the line profile as
311 follows:

312 $$\Phi_{sample} = \sum_{k=1}^{n} \left(C_{sample} \times L\right)_k \quad (3)$$

313 where C_{sample} is the ^{4}He concentration (atoms cm^{-3}) and L is the pixel width of ^{4}He (cm). This
314 method enables direct quantification of the SW-^{4}He fluence to the grain surface.

315 The SW-^{4}He fluences of the mineral grains are summarized in Table 3. The SW-
316 ^{4}He fluences for the ferrihydrite grains in Areas 4 and 5 are (58.4 ± 2.2) × 10^{16} and (3.0 ± 0.2)
317 × 10^{16} atoms cm^{-2}, respectively. Two ferrihydrite grains in Areas 4 and 5 were analyzed in the

same analytical session, with one exhibiting the highest $^{4}He^{+}$ intensity and the other a relatively low $^{4}He^{+}$ intensity. Similar $^{56}Fe^{2+}$ signal emissions, a major element of ferrihydrite, were measured from the two grains (Figs 6, 7). Therefore, the differences of $^{4}He^{+}$ intensity are not artifact and calculated ^{4}He concentration in Fig. 6c is 26 times higher than that in Fig. 7g. These results suggest that the ferrihydrite in Area 4 has the highest SW-^{4}He fluence. The SW-^{4}He fluences for the Fe-Ni metal grains range from (3.7 ± 0.8) to (11.5 ± 1.7) × 10^{16} atoms cm^{-2}. The troilite grain in Area 6 has a fluence of (5.6 ± 0.9) × 10^{16} atoms cm^{-2}. The pyroxene and olivine have fluences of (2.7 ± 0.2) and (2.9 ± 0.5) × 10^{16} atoms cm^{-2}, respectively. These values range from 2.7 × 10^{16} to 58.4 × 10^{16} atoms cm^{-2}, representing an approximately 20-fold difference in the SW-^{4}He fluence. Because SW-^{4}He in minerals may not be quantitatively retained in regolith samples (e.g., Signer et al. 1977), it should be noted that the ^{4}He fluences obtained in this study represent lower limits. Fe-Ni metals in gas-rich meteorites have the $^{4}He/^{20}Ne$ ratio of ~630 and $^{4}He/^{36}Ar$ ratio of ~30,000 (Murer et al. 1997), nearly identical to the SW ratios of 648 and 27,300, respectively (Heber et al. 2009). The bulk $^{4}He/^{20}Ne$ ratio in NWA 801 is 458 (Obase et al. 2021), which indicates at least ~30% of ^{4}He escaped from NWA 801. Thus, the ^{4}He loss of the individual grains, especially Fe-Ni metal grains, is relatively small so we do not consider ^{4}He loss in this discussion.

Based on these large variations in SW-^{4}He fluence, we can estimate the SW irradiation duration for each mineral grain. Assuming 1/π SW exposure owing to the rotation

of the parent body, the SW irradiation duration, T (yr), is calculated as follows:

$$T = \Phi_{sample}/(\varphi_{pb} \times \frac{1}{\pi}) \quad (4)$$

The SW flux φ_r (atoms cm^{-2} yr^{-1}) decreases with the square of the distance, r (astronomical unit: au), from the Sun (Adhikari et al., 2014). The SW flux at the parent body φ_{pb} (atoms cm^{-2} yr^{-1}) is calculated as

$$\varphi_{pb} = \varphi_{1au} \times \frac{1}{r^2} \quad (5)$$

Obase and Nakashima (2023) showed that the SW flux recorded in solar-gas-rich meteorites is comparable to the current levels. The present SW-^{4}He flux at 1 au (φ_{1au}) is 3.57 × 10^{14} atoms cm^{-2} yr^{-1} (Heber et al., 2009). The heliocentric distance of the CR chondrite parent body during SW irradiation might have been between the current main asteroid belt (2.2–3.3 au; DeMeo and Carry, 2014) and the presumed formation region of the CR chondrite parent body (4 au; Desch et al., 2018). The calculated SW irradiation durations range from 1.1 to 25 kyr at 2.2 au, 2.6 to 56 kyr at 3.3 au, and 3.8 to 82 kyr at 4 au (Fig. 9, Table 3).

The SW irradiation durations represent the residence time of the individual mineral grains on the top surface of the parent body, reflecting the timescale of local mixing on a millimeter-scale in its regolith. If irradiation occurred at 4 au, the residence times of the seven out of the eight individual mineral grains are 3.8–16 kyr, which is consistent with the ranges observed for Ryugu samples (≤10 kyr; Okazaki et al., 2023) and lunar regolith (2.0–13 kyr; Signer et al., 1977; Li et al., 2023). These estimated SW irradiation durations suggest that

356 the typical timescale of millimeter-scale regolith mixing on the parent body was about ten
357 thousand years. The high ^{4}He fluence for the ferrihydrite grain in Area 4 (Fig. 6) suggests a
358 SW irradiation duration of 82 kyr, which is more than ten times longer than that of the other
359 grains. This exceptionally high ^{4}He fluence suggests that the local mixing process lasted longer
360 than that for the other grains. Additionally, the long residence time may indicate that this is an
361 exotic regolith grain incorporated from a location where the mixing process is less frequent. If
362 this is indeed the case, this implies that there is a horizontal transportation mechanism for
363 regolith (e.g., electrostatic levitation; Lee, 1996). Such large variations in regolith mixing
364 frequencies, over several tens of times, have been observed on the surface of the asteroid Vesta
365 (Denevi et al., 2016).
366
367 **5. CONCLUSIONS**
368 We presented a novel technique for observing past SW-implanted ^{4}He from
369 individual mineral grains in meteorites and a method for quantifying SW-^{4}He fluence within
370 them. *In situ* ^{4}He isotope imaging with LIMAS, applied to the CR2 chondrite NWA 801,
371 provided the first direct evidence of SW implantation in individual grains of a solar-gas-rich
372 meteorite. The isotope images of Fe-Ni metal, ferrihydrite, olivine, pyroxene, and troilite grains
373 showed that ^{4}He is detected along grain interfaces, indicating its presence at depths shallower
374 than 100 nm from the grain surfaces. These results demonstrated that SW implantation

occurred in the individual grains. Additionally, the existence of SW-^{4}He in the ferrihydrite suggested two possibilities: either the implanted ^{4}He has survived in the ferrihydrite formed by terrestrial weathering of metal, or that formed through aqueous alteration on the parent body before SW exposure. The SW-^{4}He fluence of the mineral grains ranged from (2.7 to 58) × 10^{16} atoms cm^{-2}. Assuming irradiation occurred at 4 au, this corresponds to SW irradiation durations ranging from 3.8 to 82 kyr, representing the residence time of the individual mineral grains on the surface of the parent body. The residence times of most mineral grains suggest that the local mixing process on the parent body typically occurred with a frequency of about ten thousand years.

ACKNOWLEDGEMENTS

We thank Noriyuki Kawasaki for constructive discussions and technical assistance with sample preparation and SEM observations. We are grateful to Marissa Tremblay, Moshammat Mijjum, and Rainer Wieler for their constructive comments and suggestions. We are also grateful to associate editor Marc Caffee for the effective handling of our manuscript. This work was financially supported by JSPS KAKENHI grants (S.W., K.B., and H.Y.).

REFERENCES

Adhikari L., Zank G. P., Hu Q. and Dosch A. (2014) Turbulence transport modeling of the temporal outer heliosphere. *ApJ* **793**, 52.

Bajo K.-I., Kawasaki N., Sakaguchi I., Suzuki T. T., Itose S., Matsuya M., Ishihara M., Uchino K. and Yurimoto H. (2024) In Situ Helium Isotope Microimaging of Meteorites. *Anal. Chem.*

Bajo K.-I., Olinger C. T., Jurewicz A. J. G., Burnett D. S., Sakaguchi I., Suzuki T., Itose S., Ishihara M., Uchino K., Wieler R. and Yurimoto H. (2015) Depth profiling analysis of solar wind helium collected in diamond-like carbon film from Genesis. *Geochem. J.* **49**, 559–566.

Bajo K.-I., Itose S., Matsuya M., Ishihara M., Uchino K., Kudo M., Sakaguchi I. and Yurimoto H. (2016) High spatial resolution imaging of helium isotope by TOF-SNMS. *Surf. Interface Anal.* **48**, 1190–1193.

Becker R. H., Schlutter D. J., Rider P. E. and Pepin R. O. (1998) An acid-etch study of the Kapoeta achondrite: Implications for the argon-36/argon-38 ratio in the solar wind. *Meteorit. Planet. Sci.* **33**, 109–113.

Bischoff A., Palme H., Ash R. D., Clayton R. N., Schultz L., Herpers U., Stöffler D., Grady M. M., Pillinger C. T., Spettel B., Weber H., Grund T., Endreβ M. and Weber D. (1993) Paired Renazzo-type (CR) carbonaceous chondrites from the Sahara. *Geochim. Cosmochim. Acta* **57**, 1587–1603.

Bland, P.A., Zolensky, M.E., Benedix, G.K. and Sephton, M.A. (2006) Weathering of chondritic meteorites. *Meteorites and the early solar system II*, 853–867.

Charles C. R. J., Robin P.-Y. F., Davis D. W. and McCausland P. J. A. (2018) Shapes of chondrules determined from the petrofabric of the CR2 chondrite NWA 801. *Meteorit. Planet. Sci.* **53**, 935–951.

Connolly H. C. Jr, Smith C., Benedix G., Folco L., Righter K., Zipfel J., Yamaguchi A. and Aoudjehane H. C. (2007) Meteoritical Bulletin, no. 92. *Meteoritics & Planetary Science* **42**, 1647–1694.

DeMeo F. E. and Carry B. (2014) Solar System evolution from compositional mapping of the asteroid belt. *Nature* **505**, 629–634.

Denevi B. W., Beck A. W., Coman E. I., Thomson B. J., Ammannito E., Blewett D. T., Sunshine J. M., De Sanctis M. C., Li J.-Y., Marchi S., Mittlefehldt D. W., Petro N. E., Raymond C. A. and Russell C. T. (2016) Global variations in regolith properties on asteroid Vesta from Dawn's low-altitude mapping orbit. *Meteorit. Planet. Sci.* **51**, 2366–2386.

Desch S. J., Kalyaan A. and O'D. Alexander C. M. (2018) The Effect of Jupiter's Formation on the Distribution of Refractory Elements and Inclusions in Meteorites. *ApJS* **238**, 11.Ebata S., Ishihara M., Uchino K., Itose S., Matsuya M., Kudo M., Bajo K. I. and

Yurimoto H. (2012) Development of laser ionization mass nanoscope (LIMAS). *Surf. Interface Anal.* **44**, 635–640.

Eberhardt P., Geiss J. and Grögler N. (1965) Further evidence on the origin of trapped gases in the meteorite Khor Temiki. *Journal of Geophysical Research* **70**, 4375–4378.

Futagami, T., Ozima, M. and Nakamura, Y. (1990) Helium ion implantation into minerals. *Earth and planetary science letters*, **101**, 63–67.

Geiss J., Buehler F., Cerutti H., Eberhardt P. and Filleux C. (1972) Solar wind composition experiment. *Apollo 16 Preliminary Science Report* **14**, 1–10.

Grimberg, A., Baur, H., Bühler, F., Bochsler, P. and Wieler, R. (2008) Solar wind helium, neon, and argon isotopic and elemental composition: Data from the metallic glass flown on NASA's Genesis mission. *Geochim. Cosmochim. Acta* **72**, 626–645.

Hashiguchi, M., Kobayashi, S. and Yurimoto, H. (2013) In situ observation of D-rich carbonaceous globules embedded in NWA 801 CR2 chondrite. *Geochim. Cosmochim. Acta.* **122,** 306-323.

Heber V. S., Wieler R., Baur H., Olinger C., Friedmann T. A. and Burnett D. S. (2009) Noble gas composition of the solar wind as collected by the Genesis mission. *Geochim. Cosmochim. Acta* **73**, 7414–7432.

Hintenberger H., Weber H. and Takaoka N. (1971) Concentration and Isotopic Abundances of the Rare Gases in Lunar Matter. In pp. 230–230.

Hintenberger H., Weber H. W., Voshage H., Wänke H., Begemann F. and Wlotzka F. (1970) Concentrations and isotopic abundances of the rare gases, hydrogen and nitrogen in lunar matter. *Geochimica et Cosmochimica Acta Supplement* **1**, 1269.

Kuhlman, K.R., Sridharan, K. and Kvit, A. (2015) Simulation of solar wind space weathering in orthopyroxene. *Planet. Space Sci.* **115**, 110–114.

Lee P. (1996) Dust Levitation on Asteroids. *Icarus* **124**, 181–194.

Li J., Li Z., Huang Z., Li T., Guo D., Liu H., Fan G., Qin M., Lei L., Zhou X., Wang H., Wang K., Gao X., Yu A., Liu R., Zhang J., Deng L., He S., Wu Y. and Qiu L. (2023) Weak influence of the secondary surface processes on the regolith of Chang'E-5 landing site. *Communications Earth & Environment* **4**, 1–9.

Lipschutz M. E., Wolf S. F., Vogt S., Michlovich E., Lindstrom M. M., Zolensky M. E.,

Mittlefehldt D. W., Satterwhite C., Schultz L., Loeken T., Scherer P., Dodd R. T., Sears D. W. G., Benoit P. H., Wacker J. F., Burns R. G. and Fisher D. S. (1993) Consortium study of the unusual H chondrite regolith breccia, Noblesville. *Meteoritics* **28**, 528–537.

Murer C. A., Baur H., Signer P. and Wieler R. (1997) Helium, neon, and argon abundances in the solar wind: In vacuo etching of meteoritic iron-nickel. *Geochim. Cosmochim. Acta* **61**, 1303–1314.

Nagata K., Bajo K. I., Itose S., Matsuya M., Ishihara M., Uchino K. and Yurimoto H. (2019) Aberration-corrected focused ion beam for time-of-flight secondary neutral mass spectrometry. *Appl. Phys. Express* **12**.

Nakamura T., Nagao K., Metzler K. and Takaoka N. (1999) Heterogeneous distribution of solar and cosmogenic noble gases in CM chondrites and implications for the formation of CM parent bodies. *Geochim. Cosmochim. Acta* **63**, 257–273.

Nakashima D., Matsuda S., Iio H., Bajo K., Ebisawa N. and Nagao K. (2009) Noble Gases in the NWA 852/801 CR2 Chondrites. *LPSC abstract*. In p. 1661.

Noguchi T. (1994) Petrology and mineralogy of the Coolidge meteorite (CV4). *Proc. NIPR Symp. Antarct. Meteorites* **7**, 42–72.

Obase T. and Nakashima D. (2023) Past solar wind flux recorded in solar-gas-rich meteorites. *Icarus* **389**, 115290.

Obase T., Nakashima D., Choi J., Enokido Y., Matsumoto M. and Nakamura T. (2021) Water-susceptible primordial noble gas components in less-altered CR chondrites: A possible link to cometary materials. *Geochim. Cosmochim. Acta* **312**, 75–105.

Okazaki R., Marty B., Busemann H., Hashizume K., Gilmour J. D., Meshik A., Yada T., Kitajima F., Broadley M. W., Byrne D., Füri E., Riebe M. E. I., Krietsch D., Maden C., Ishida A., Clay P., Crowther S. A., Fawcett L., Lawton T., Pravdivtseva O., Miura Y. N., Park J., Bajo K.-I., Takano Y., Yamada K., Kawagucci S., Matsui Y., Yamamoto M., Righter K., Sakai S., Iwata N., Shirai N., Sekimoto S., Inagaki M., Ebihara M., Yokochi R., Nishiizumi K., Nagao K., Lee J. I., Kano A., Caffee M. W., Uemura R., Nakamura T., Naraoka H., Noguchi T., Yabuta H., Yurimoto H., Tachibana S., Sawada H., Sakamoto K., Abe M., Arakawa M., Fujii A., Hayakawa M., Hirata Naoyuki, Hirata Naru, Honda R., Honda C., Hosoda S., Iijima Y.-I., Ikeda H., Ishiguro M., Ishihara Y., Iwata T., Kawahara K., Kikuchi S., Kitazato K., Matsumoto K., Matsuoka M., Michikami T., Mimasu Y., Miura A., Morota T., Nakazawa S., Namiki N., Noda

H., Noguchi R., Ogawa N., Ogawa K., Okada T., Okamoto C., Ono G., Ozaki M., Saiki T., Sakatani N., Senshu H., Shimaki Y., Shirai K., Sugita S., Takei Y., Takeuchi H., Tanaka S., Tatsumi E., Terui F., Tsukizaki R., Wada K., Yamada M., Yamada T., Yamamoto Y., Yano H., Yokota Y., Yoshihara K., Yoshikawa M., Yoshikawa K., Furuya S., Hatakeda K., Hayashi T., Hitomi Y., Kumagai K., Miyazaki A., Nakato A., Nishimura M., Soejima H., Iwamae A., Yamamoto D., Yogata K., Yoshitake M., Fukai R., Usui T., Connolly H. C. Jr, Lauretta D., Watanabe S.-I. and Tsuda Y. (2023) Noble gases and nitrogen in samples of asteroid Ryugu record its volatile sources and recent surface evolution. *Science* **379**, eabo0431.

Okumura D., Toyoda M., Ishihara M. and Katakuse I. (2004) A compact sector-type multi-turn time-of-flight mass spectrometer 'MULTUM II.' *Nucl. Instrum. Methods Phys. Res. A* **519**, 331–337.

Riebe M. E. I., Busemann H., Wieler R. and Maden C. (2017) Closed System Step Etching of CI chondrite Ivuna reveals primordial noble gases in the HF-solubles. *Geochim. Cosmochim. Acta* **205**, 65–83.

Scherer P. and Schultz L. (2000) Noble gas record, collisional history, and pairing of CV, CO, CK, and other carbonaceous chondrites. *Meteorit. Planet. Sci.* **35**, 145–153.

Scherer P., Loeken T. and Schultz L. (1994) Noble gases in chondrites found in hot deserts. *Meteoritics* **29**, 529.

Signer P., Baur H., Derksen U., Etique P., Funk H., Rn P. H. and Wieler R. (1977) Helium, neon, and argon records of lunar soil evolution. In *Proceedings of Lunar Science Conference 8th* Lunar Science Conference 8th. pp. 3657–3683.

Stelzner, T.H., Heide, K., Bischoff, A., Weber, D., Scherer, P., Schultz, L., Happel, M., Schrön, W., Neupert, U., Michel, R. and Clayton, R.N. (1999) An interdisciplinary study of weathering effects in ordinary chondrites from the Acfer region, Algeria. *Meteorit. Planet. Sci.* **34**, 787–794.

Tomeoka K. and Buseck P. R. (1988) Matrix mineralogy of the Orgueil CI carbonaceous chondrite. *Geochim. Cosmochim. Acta* **52**, 1627–1640.

Tonotani A., Bajo K. I., Itose S., Ishihara M., Uchino K. and Yurimoto H. (2016) Evaluation of multi-turn time-of-flight mass spectrum of laser ionization mass nanoscope. *Surf. Interface Anal.* **48**, 1122–1126.

Wiens, R.C., Bochsler, P., Burnett, D.S. and Wimmer-Schweingruber, R.F. (2004) Solar and

525 solar wind isotopic compositions. *Earth and Planetary Science Letters*, **226**, 549–565.

526 Wieler R., Baur H., Pedroni A., Signer P. and Pellas P. (1989) Exposure history of the
527 regolithic chondrite Fayetteville: I. Solar-gas-rich matrix. *Geochim. Cosmochim. Acta*
528 **53**, 1441–1448.

529 Wieler R., Pedroni A. and Leya I. (2000) Cosmogenic neon in mineral separates from
530 Kapoeta: No evidence for an irradiation of its parent body regolith by an early active
531 Sun. *Meteorit. Planet. Sci.* **35**, 251–257.

532 Ziegler, J. F., Biersack, J. P., Ziegler, M. D., SRIM, The Stopping and Range of Ions in
533 Matter. (http://www.srim.org) 2012.

534

535

536 **FIGURES**

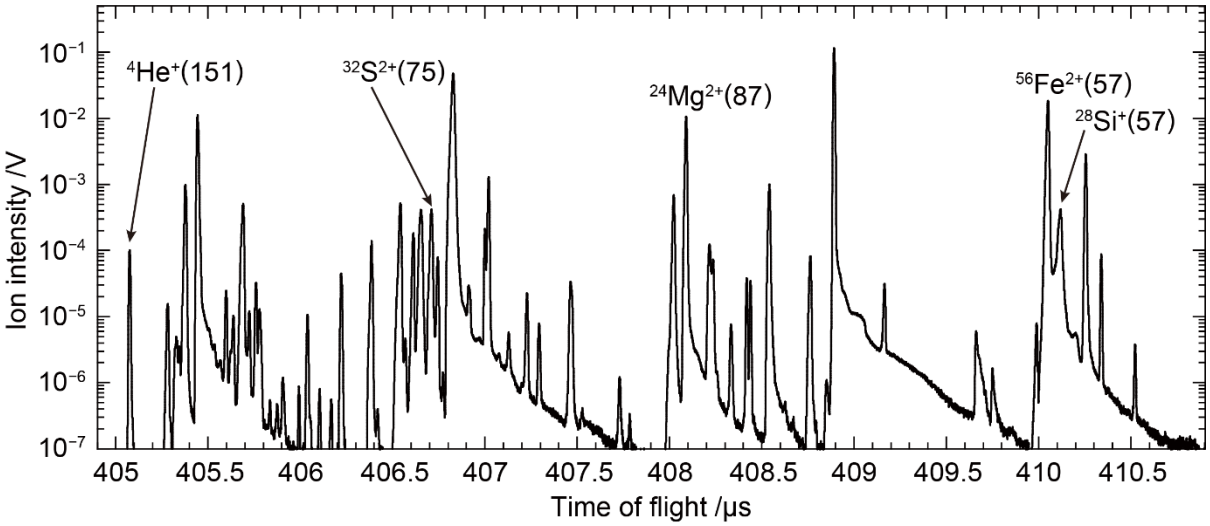

537

538 **Figure 1.** TOF mass spectrum of Area 4 of the NWA 801 sample shown in Fig. 6b. The arrows
539 indicate the measured ion species, where the numbers in parentheses indicate the numbers of
540 laps for each ion in MULTUM-II.

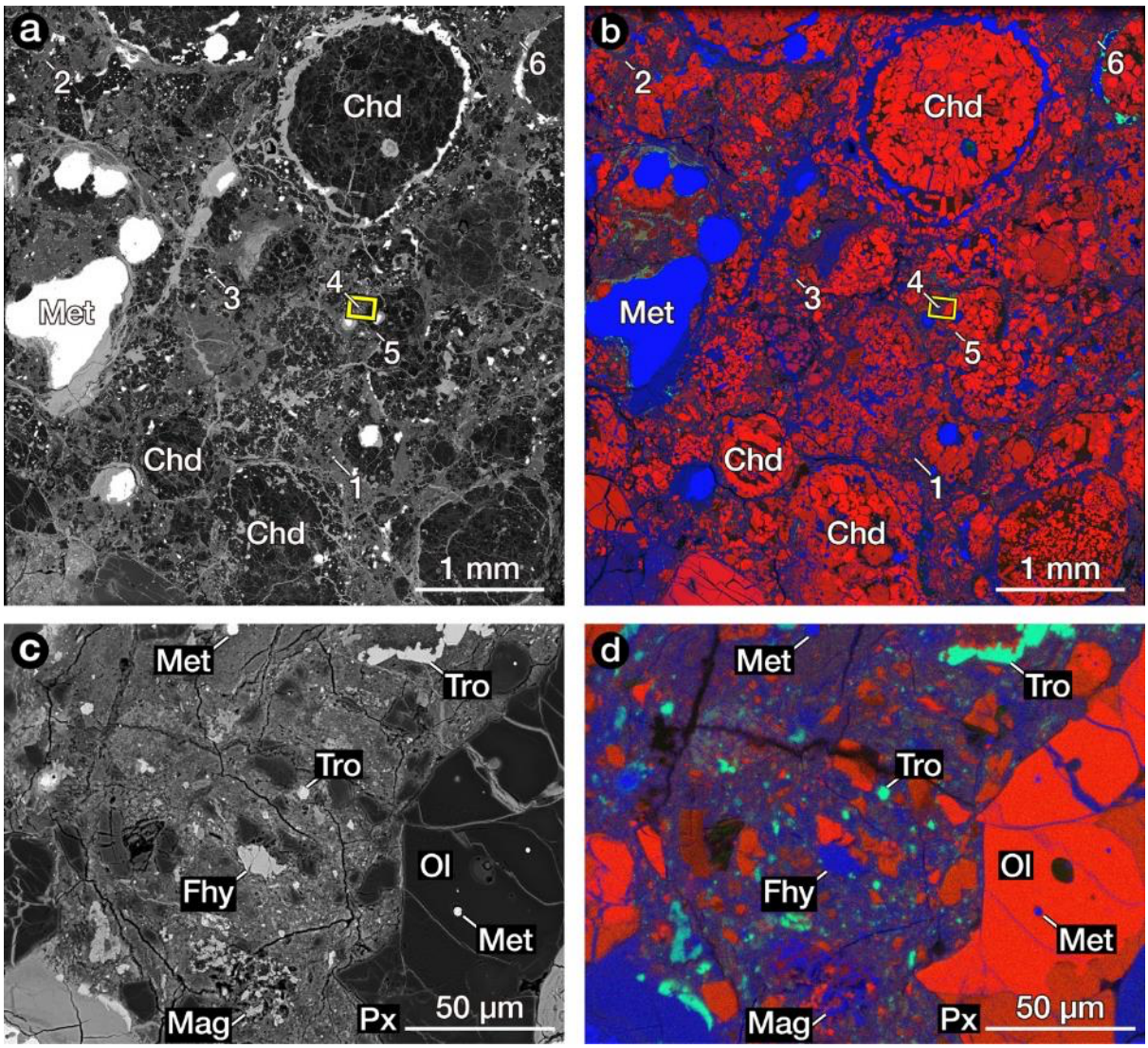

Figure 2. (a) BSE image of a section of NWA 801. (b) Composite X-ray elemental map of the area shown in (a), with Mg (red), Si (green), and Fe (blue). (c) Magnified BSE image of the area indicated by yellow boxes in (a) and (b). (d) Composite X-ray elemental map of the area shown in (c), with Mg (red), Si (green), and Fe (blue). Numbers 1–6 correspond to locations shown in Figs. 3–8, respectively. Abbreviations: Chd, chondrule; Fhy, ferrihydrite; Mag, magnetite; Met, Fe-Ni metal; Ol, olivine; Px, pyroxene; Tro, troilite.

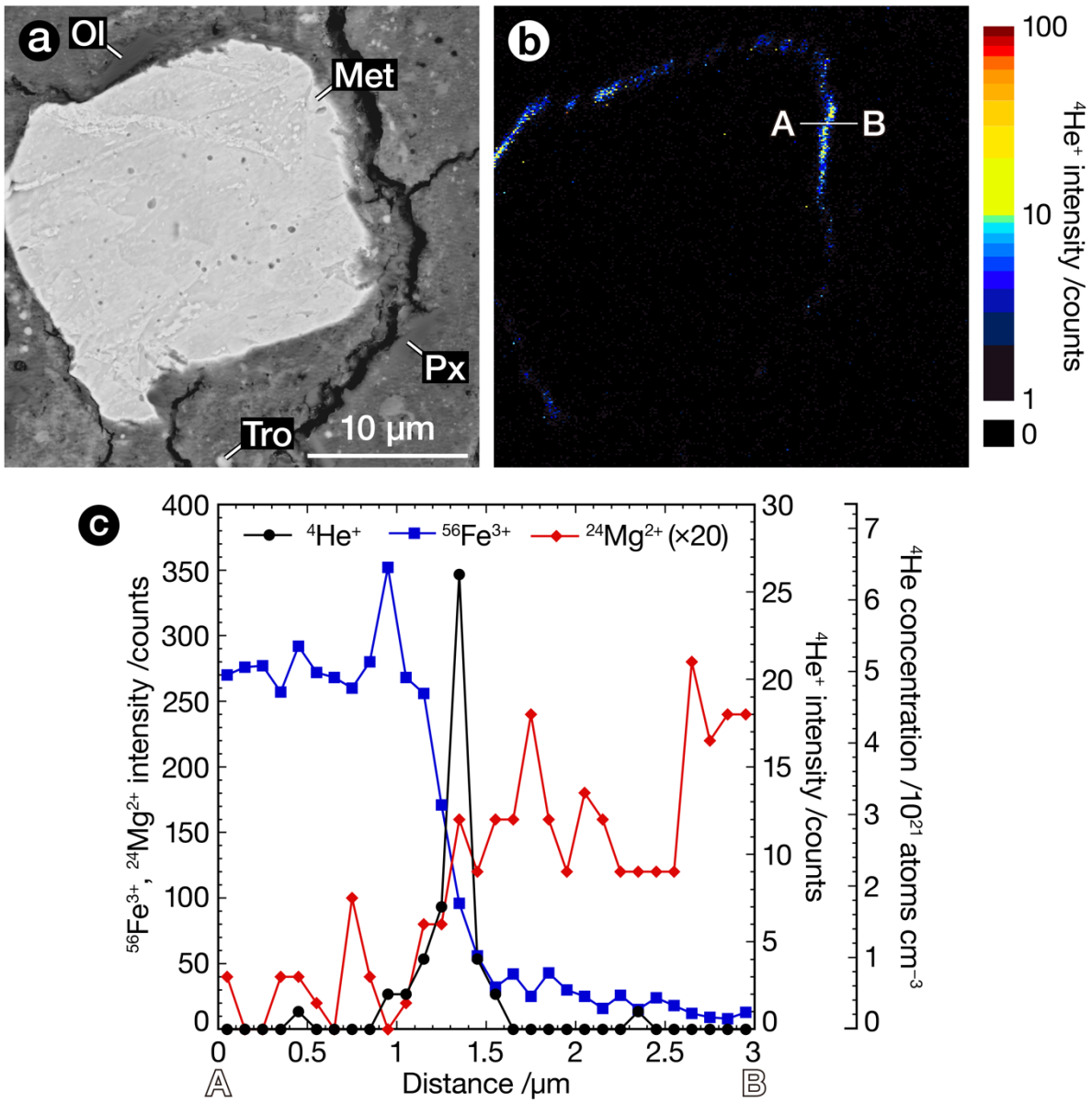

548

549 **Figure 3.** (a) BSE image of Area 1. (b) $^{4}He^{+}$ image of Area 1. (c) Line profiles for $^{4}He^{+}$,
550 $^{56}Fe^{2+}$, and $^{24}Mg^{2+}$ along traverse A–B across the metal interface. Abbreviations: Met, Fe-Ni
551 metal; Ol, olivine; Px, pyroxene; Tro, troilite.

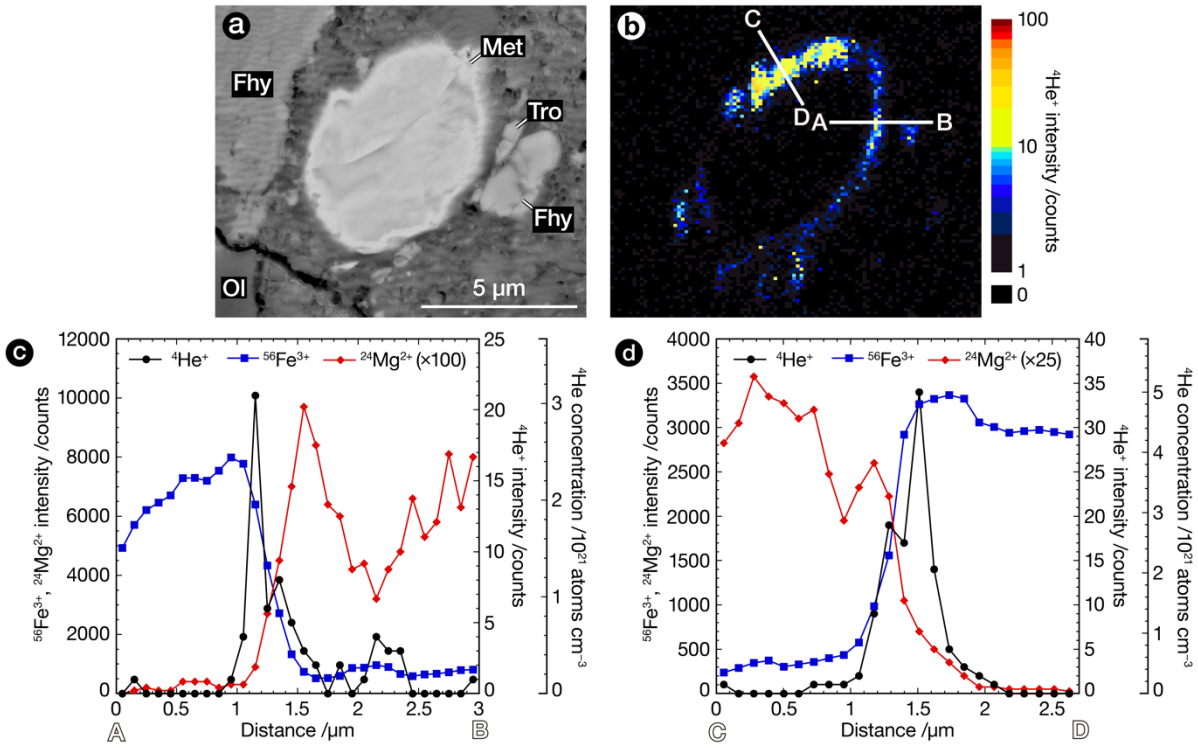

552

553 **Figure 4.** (a) BSE image of Area 2. (b) $^{4}He^{+}$ image of Area 2. (c) Line profiles for $^{4}He^{+}$,
554 $^{56}Fe^{2+}$, and $^{24}Mg^{2+}$ along traverse A–B across the metal interface in (b). (d) Line profiles for
555 $^{4}He^{+}$, $^{56}Fe^{2+}$, and $^{24}Mg^{2+}$ along traverse C–D across the metal interface in (b). Abbreviations:
556 Fhy, ferrihydrite; Met, Fe-Ni metal; Ol, olivine; Tro, troilite.

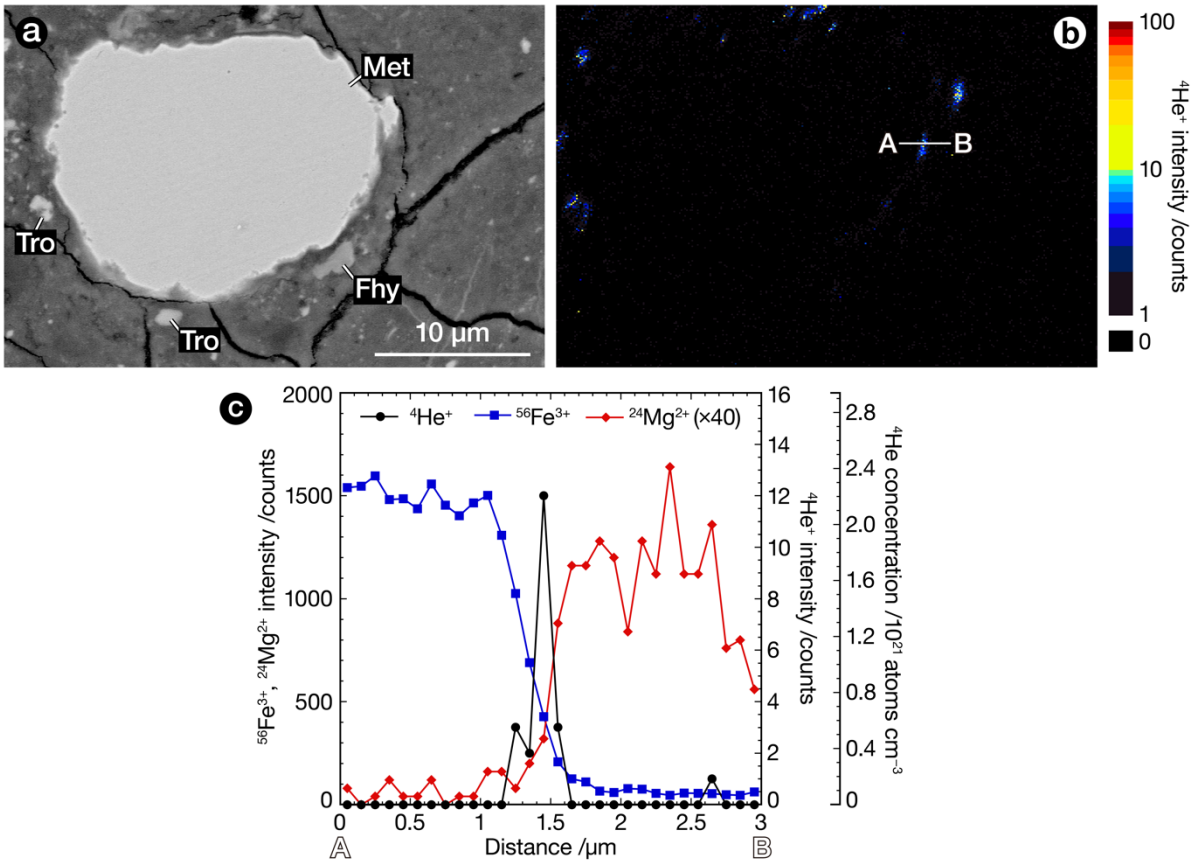

557

558 **Figure 5.** (a) BSE image of Area 3. (b) $^{4}He^{+}$ image of Area 3. (c) Line profiles for $^{4}He^{+}$,
559 $^{56}Fe^{2+}$, and $^{24}Mg^{2+}$ along traverse A–B across the metal interface in (b). Abbreviations: Fhy,
560 ferrihydrite; Met, Fe-Ni metal; Tro, troilite.

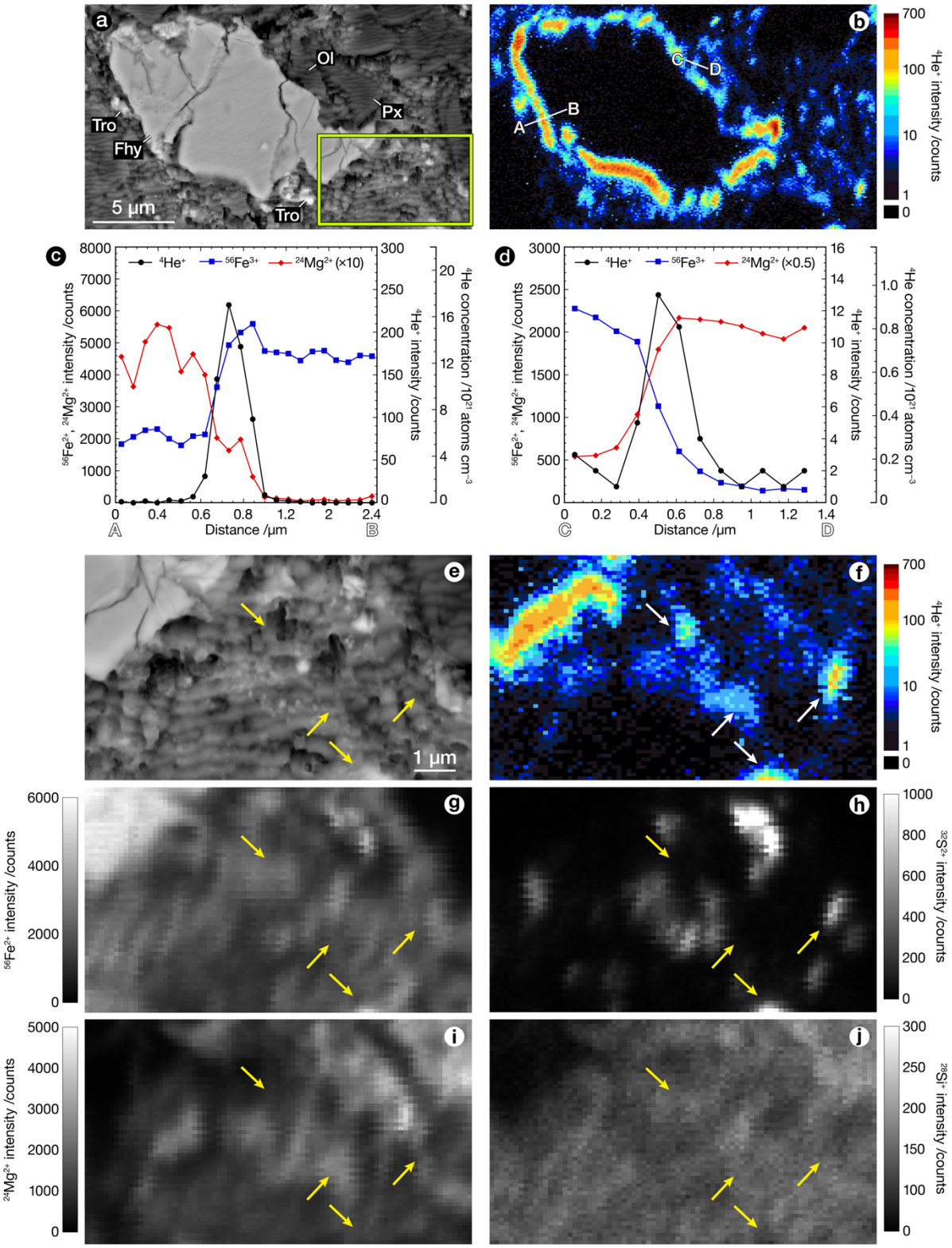

Figure 6. (a) BSE image of Area 4. (b) $^{4}He^{+}$ image of Area 4. (c) Line profiles for $^{4}He^{+}$, $^{56}Fe^{2+}$, and $^{24}Mg^{2+}$ along traverse A–B across the ferrihydrite interface in (b). (d) Line profiles for $^{4}He^{+}$, $^{56}Fe^{2+}$, and $^{24}Mg^{2+}$ ion intensities along traverse C–D across the pyroxene interface in (b). (e) Magnified BSE image of Area 4 delineated by the yellow box in (a). (f) $^{4}He^{+}$ image of Fig. 6e. (g) $^{56}Fe^{2+}$ image of Fig. 6e. (h) $^{32}S^{2+}$ image of Fig. 6e. (i) $^{24}Mg^{2+}$ image of Fig. 6e.

(j) $^{28}Si^{2+}$ image of Fig. 6e. The yellow arrows in (e) and (g)–(j) and white arrows in (f) indicate the locations of $^{4}He^{+}$ enriched spots in the groundmass. Abbreviations: Fhy, ferrihydrite; Ol, olivine; Px, pyroxene; Tro, troilite.

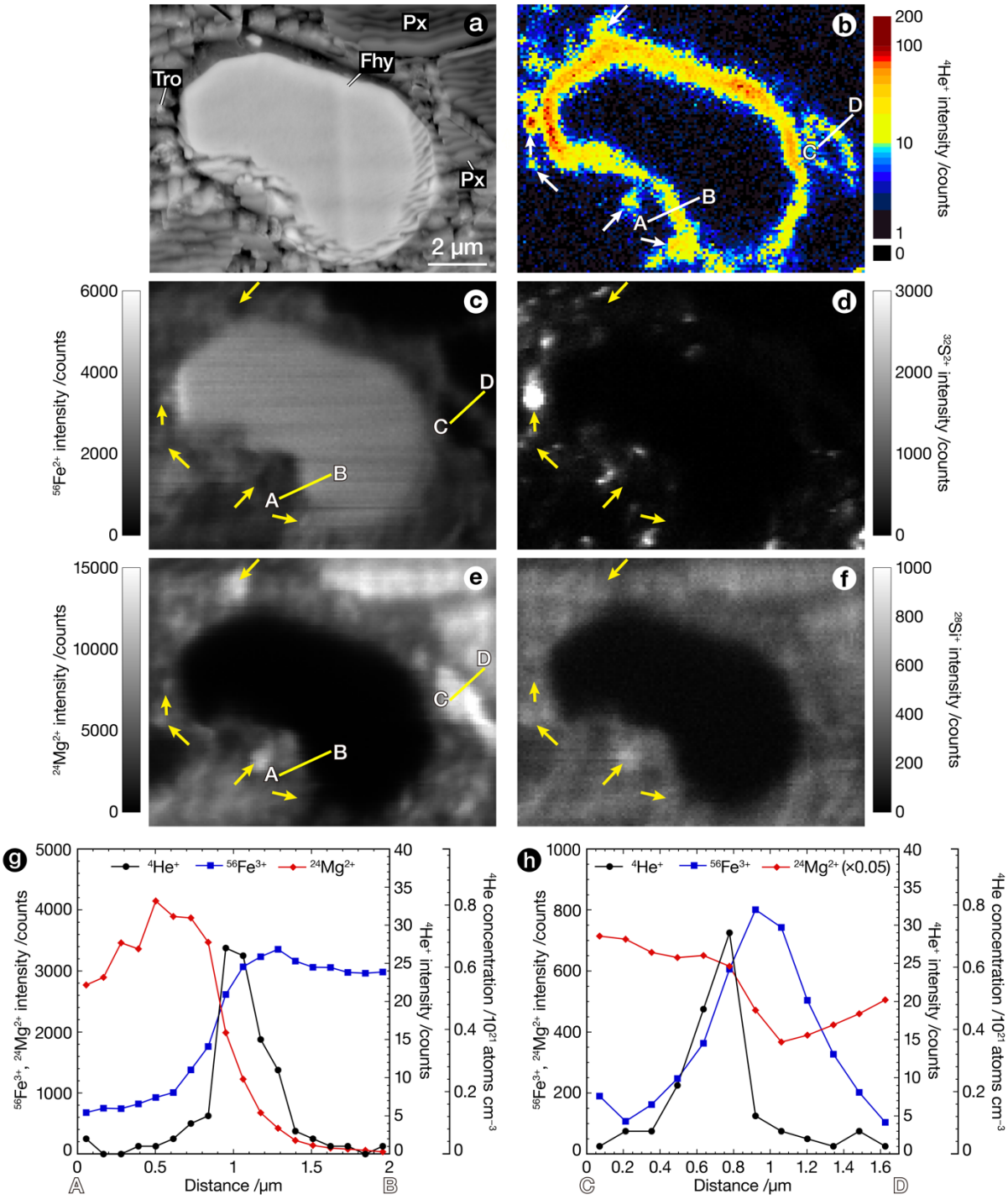

Figure 7. (a) BSE image of Area 5. (b) $^{4}He^{+}$ image of Area 5. (c) $^{56}Fe^{2+}$ image of Area 5. (d) $^{32}S^{2+}$ image of Fig. 7b. (e) $^{24}Mg^{2+}$ image of Fig. 7b. (f) $^{28}Si^{2+}$ image of Fig. 7b. (g) Line profiles for $^{4}He^{+}$, $^{56}Fe^{2+}$, and $^{24}Mg^{2+}$ along traverse A–B in (b). (h) Line profiles for $^{4}He^{+}$, $^{56}Fe^{2+}$, and $^{24}Mg^{2+}$ ion intensity along traverse C–D in (b). The yellow arrows in (a)–(f) indicate the locations of $^{4}He^{+}$ enriched spots in the groundmass. Abbreviations: Fhy, ferrihydrite; Px, pyroxene; Tro, troilite.

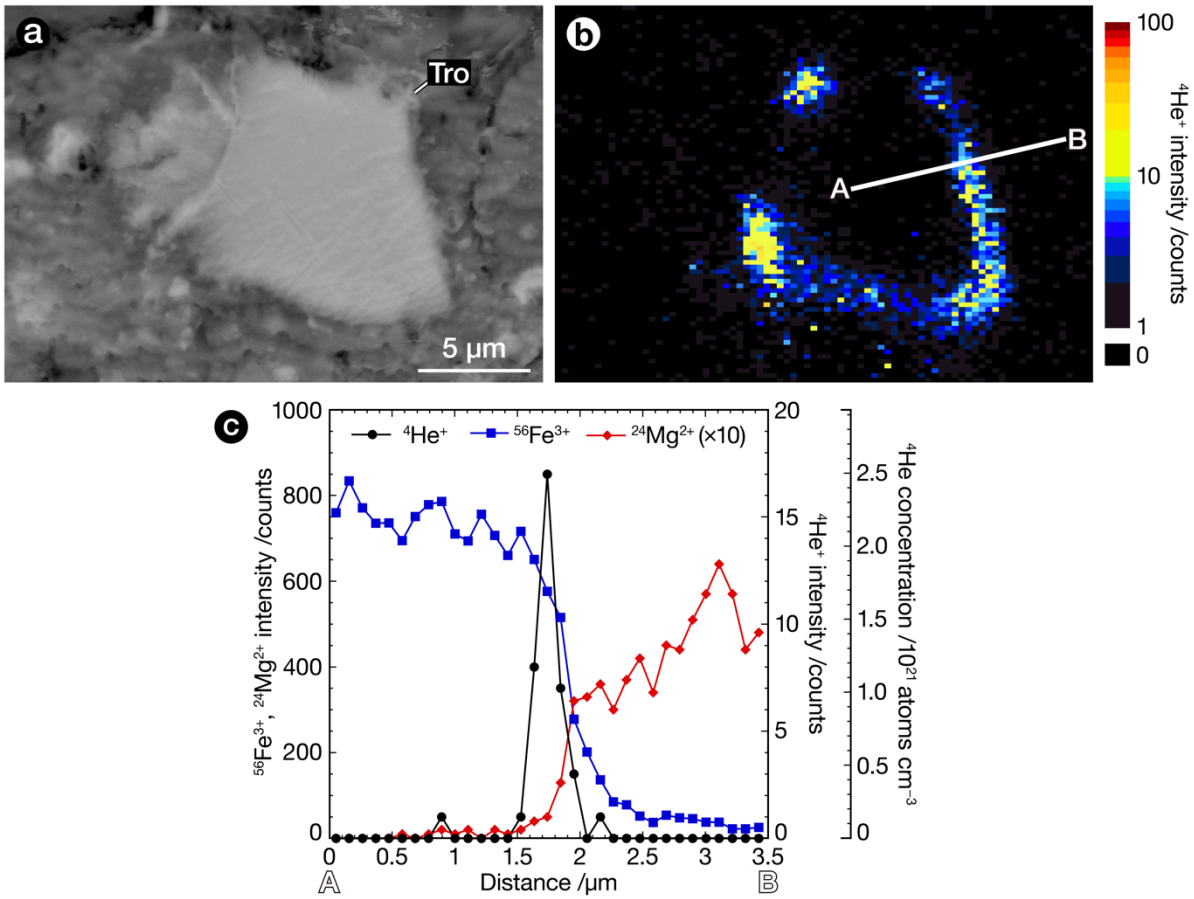

Figure 8. (a) BSE image of Area 6. (b) $^{4}He^{+}$ image of Area 6. (c) Line profiles for $^{4}He^{+}$, $^{56}Fe^{2+}$, and $^{24}Mg^{2+}$ along traverse A–B in (b). Abbreviations: Tro, troilite.

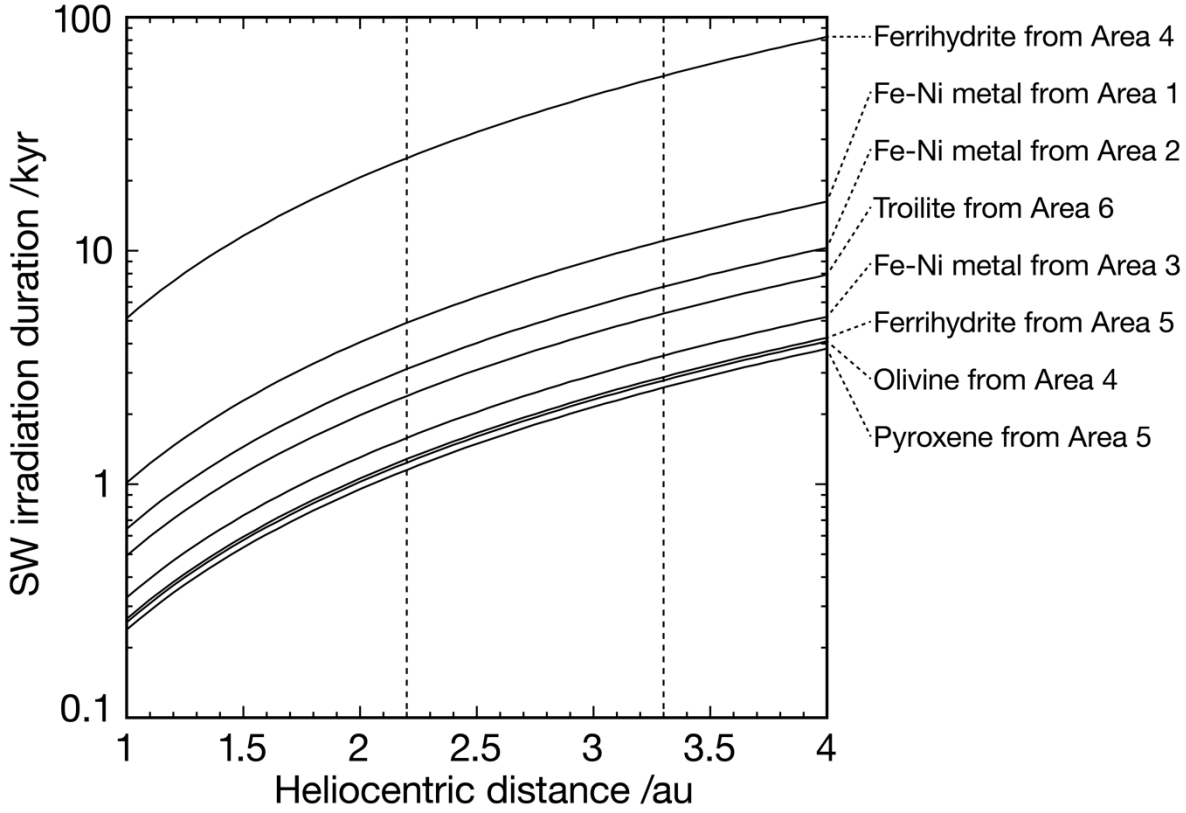

581

582 **Figure 9.** SW irradiation durations for mineral grains.

583

584 **TABLES**

585 **Table 1.** Analytical conditions for isotope imaging.

Area	Image size /μm^2	Pixels	Num. of mass scan per pixel
1	25 × 30	250 × 300	600
2	10 × 10	100 × 100	1000
3	30 × 25	300 × 250	800
4	10 × 12	100 × 120	2000
5	15 × 20	150 × 200	6000
6	8 × 8	80 × 80	1000

586

587 **Table 2.** Spatial resolutions of isotope images.

Area	Mineral	$^{4}He^{+}$ * /nm	$^{56}Fe^{2+, 3+}$ ** /nm	$^{24}Mg^{2+}$ ** /nm
1	Fe-Ni metal	100	260	240
2	Fe-Ni metal	100	260	300
3	Fe-Ni metal	100	350	220
4	Ferrihydrite	250	160	440
4	Olivine	230	270	210
5	Ferrihydrite	240	310	330
5	Pyroxene	240	300	170
6	Troilite	150	450	400

*Peak width of $^{4}He^{+}$, **16–84% width from the line scan (Figs. S1–S6)

588

589 **Table 3.** SW-^{4}He fluences and SW irradiation durations for mineral grains.

Area	Mineral	Line profile	^{4}He fluence /10^{16} atoms cm^{-2}	SW irradiation duration /kyr 2.2 au	3.3 au	4.0 au
1	Fe-Ni metal	A–B	11.5 ± 1.7	4.9 ± 0.7	11.0 ± 1.6	16.2 ± 2.4
2	Fe-Ni metal	A–B	7.3 ± 1.0	3.1 ± 0.4	7.0 ± 1.0	10.3 ± 1.4
3	Fe-Ni metal	A–B	3.7 ± 0.8	1.6 ± 0.3	3.6 ± 0.8	5.2 ± 1.1
4	Ferrihydrite	A–B	58.4 ± 2.2	24.9 ± 0.9	56.1 ± 2.1	82.4 ± 3.1
4	Olivine	C–D	2.9 ± 0.5	1.2 ± 0.2	2.8 ± 0.5	4.1 ± 0.7
5	Ferrihydrite	A–B	3.0 ± 0.2	1.3 ± 0.1	2.9 ± 0.2	4.2 ± 0.3
5	Pyroxene	C–D	2.7 ± 0.2	1.1 ± 0.1	2.6 ± 0.2	3.8 ± 0.3
6	Troilite	A–B	5.6 ± 0.9	2.4 ± 0.4	5.4 ± 0.9	7.9 ± 1.3

590 Errors in 1σ